

1           **Modulated light-activated electrochemistry at silicon**  
2           **functionalized with metal-organic frameworks towards**  
3           **addressable DNA chips**

4           *Jian Wang<sup>1</sup>, Zhao Yang<sup>1</sup>, Wei Chen<sup>1</sup>, Liping Du<sup>1</sup>, Bo Jiao<sup>2</sup>, Steffi Krause<sup>3</sup>, Ping Wang<sup>4</sup>,*  
5           *Qiuping Wei<sup>5</sup>, De-Wen Zhang<sup>1\*</sup>, Chunsheng Wu<sup>1\*</sup>*

6           <sup>1</sup>Institute of Medical Engineering, School of Basic Medical Sciences, Health Science  
7           Center, Xi'an Jiaotong University, Xi'an 710061, China

8           <sup>2</sup>School of Electronic and Information Engineering, Department of Biophysics, Xi'an  
9           Jiaotong University, Xi'an, 10049, China

10          <sup>3</sup>School of Engineering and Materials Science, Queen Mary University of London, Mile  
11          End Road, London E1 4NS, U.K.

12          <sup>4</sup>Biosensor National Special Laboratory, Key Laboratory for Biomedical Engineering of  
13          Ministry of Education, Department of Biomedical Engineering, Zhejiang University,  
14          Hangzhou 310027, China

15          <sup>5</sup>State Key Laboratory of Powder Metallurgy, School of Materials Science and Engineering,  
16          Central South University, Changsha 410083, China

17          \*Corresponding authors:

18          D. Zhang (e-mail: zhangdewen@xjtu.edu.cn)

19          C. Wu (e-mail: wuchunsheng@xjtu.edu.cn)

20          **Abstract:**

21          Modulated light-activated electrochemistry (MLAE) at semiconductor/liquid interfaces  
22          derived from light-addressable potentiometric sensor (LAPS) and light-activated  
23          electrochemistry (LAE) for addressable photoelectrochemical sensing has been  
24          proposed as a new sensor platform. In this system, a bias voltage is applied to create  
25          a depletion layer at the silicon/electrolyte interface. Meanwhile, intensity-modulated  
26          light illuminates the movable electrode to generate electron/hole pairs and causes a  
27          detectable local AC photocurrent. The AC measurement showed a higher  
28          signal-to-noise ratio (SNR) of photocurrents compared to the traditional DC response,  
29          while a steeper photocurrent-voltage (*I-V*) curve than that of LAPS with an insulating  
30          layer was obtained. Furthermore, to stabilize and functionalize the silicon substrate,  
31          metal-organic framework (MOF) nanoparticles were grown in-situ on the silicon  
32          electrode. The successful modification was validated by X-ray diffraction (XRD) and

33 scanning electron microscopy (SEM). The AC photocurrent increased as a result of  
34 the adsorption of negatively charged DNA, which contributed to the enhancement of  
35 the cathodic reduction process at the semiconductor electrodes, indicating a different  
36 response mechanism of MLAE from LAPS. The results obtained demonstrate the  
37 potential of MOF functionalized MLAE as a robust platform for light-addressable DNA  
38 chips with high sensitivity and specificity.

39 **Key words:** light-activated electrochemistry, light-addressable potentiometric sensor,  
40 metal-organic framework, DNA chip, photocurrent

## 41 **1. Introduction**

42 Electrochemical measurements with spatial resolution are essential and important for  
43 high-throughput analysis and the investigation of heterogeneous processes.  
44 Microelectrode arrays (MEAs) (Obien et al. 2015; Spira and Hai 2013) and probe-type  
45 electrodes (Macazo and White 2016; Perry et al. 2017; Polcari et al. 2016; Takahashi  
46 et al. 2012) have been proposed to achieve spatial discrimination of various analytes.  
47 MEAs require a separate sensing electrode with connecting wire for every separate  
48 spatial area, multistep fabrication processes and, hence, significant production costs.  
49 The geometrical restrictions limit the achievable density of effective working sites on  
50 the device. Probe-type electrodes, such as scanning electrochemical microscopy  
51 (SECM) (Polcari et al. 2016; Takahashi et al. 2012) and scanning ion conductance  
52 microscopy (SICM) (Macazo and White 2016; Perry et al. 2017), employ an  
53 ultramicroelectrode or nanoelectrode tip to scan in close proximity to a surface to  
54 record electrochemical information as a function of spatial location, but the tip  
55 displacement in solution may cause convective disruption of the measurement, and  
56 scanning probe techniques are inherently slow (Licht et al. 1996).

57 As a probe-less method, light-addressable potentiometric sensors (LAPSs) have  
58 been extensively employed for spatially resolved biological investigations (Hafeman  
59 et al. 1988; Wang et al. 2018; Yoshinobu et al. 2015; Yoshinobu et al. 2017). Based  
60 on an electrolyte-insulator-semiconductor (EIS) field-effect structure, a bias voltage is  
61 applied to create a depletion layer at the semiconductor/insulator interface.  
62 Meanwhile, an intensity-modulated light illuminates the substrate to generate a local  
63 AC photocurrent. The photocurrent is affected by the electrical potential difference at  
64 the solid/liquid interface. For example, the adsorption of charged molecules on a  
65 sensor surface can alter the interfacial potential and thereby affect the photocurrent  
66 output (Wu et al. 2016). An advantage of LAPS is the use of light induced local  
67 photocurrents to achieve spatial confinement without the need of a physical probe. In  
68 addition, the construction is simple and inexpensive with a single sensor and fewer  
69 electrical contacts compared to the conventional pre-determined array scheme.  
70 However, the intrinsic drawback of LAPS is that no DC currents cross the interface,  
71 which inhibits the electrochemical reactivity of the interface and therefore the scope of  
72 the technology is limited to potentiometric measurements (Poghossian and Schöning

73 2014; Wu et al. 2019). Light-addressable electrochemistry or light-activated  
74 electrochemistry (LAE) (Choudhury et al. 2017; Seo et al. 2018; Vogel et al. 2019;  
75 Yang et al. 2016; Yang et al. 2018), which is based on an electrolyte-semiconductor  
76 (ES) structure, overcomes this limitation. Light with constant intensity is used to  
77 generate electron-hole pairs in a semiconductor biased towards depletion resulting in  
78 a DC photocurrent output. This system allows local faradaic currents to cross the ES  
79 interface, which broadens the applications to amperometric detection principles.

80 Recently, the ES structure has also been demonstrated to be suitable for AC  
81 photocurrent measurements with spatial addressability (Tu et al. 2018; Wu et al. 2019;  
82 Zhang et al. 2017b). The AC photocurrent consists of both, depletion layer charging  
83 current and redox current, which is promising for integrating the merits of both LAPS  
84 and LAE. The reported sensors with high resolution are based on metal oxide  
85 semiconductors such as ITO (Wu et al. 2019; Zhang et al. 2017b) and ZnO (Tu et al.  
86 2018). Silicon is a preferred semiconductor for the development of  
87 photoelectrochemical devices due to its narrow band gap, high charge carrier mobility,  
88 abundance and well-established fabrication methods in the semiconductor industry.  
89 However, the electrochemistry of bare silicon has proven to be very challenging as it  
90 is not stable in aqueous media. In DC photocurrent measurement systems, silicon  
91 substrates are usually protected with self-assembled organic monolayers (Choudhury  
92 et al. 2017; Yang et al. 2016; Yang et al. 2018).

93 In this study, we investigate the possibility of stable nanoparticle modified silicon as  
94 the electrode for spatially resolved AC photocurrent measurements. To stabilize and  
95 functionalize the electrode, metal-organic frameworks (MOFs), which are constructed  
96 by metal ions/clusters and organic bridging ligands, were prepared on the silicon  
97 surface. Due to their prominent properties of flexible porosity, large surface area and  
98 facilely tailorable functionality, MOFs have been widely applied as a robust platform  
99 for surface immobilization of biosensing elements in the construction of  
100 electrochemical biosensors (Ma et al. 2013; Meng et al. 2018; Meng et al. 2017;  
101 Zhang et al. 2017a). For instance, they have been used as a matrix for enzyme  
102 immobilization on electrodes for highly sensitive electrochemical enzymatic detection  
103 (Ma et al. 2013; Zhang et al. 2017a). MOF-based electrochemical sensors for the  
104 detection of DNA sequences are very rare thus far (Campbell and Dincă 2017).  
105 Herein, we report modulated light-activated electrochemistry (MLAE) on the basis of  
106 MOF nanoparticle modified silicon electrodes for multi-spot label-free DNA sensing.  
107 The simple and low-cost device uses intensity-modulated light to irradiate a movable  
108 electrolyte-silicon structure to generate local AC photocurrents. The photocurrent was  
109 monitored using a lock-in amplifier. UIO-66-NH<sub>2</sub>, which is a class of MOFs made of  
110 zirconium ions and terephthalate ligands, was deposited on silicon in-situ as the  
111 immobilization and sensing matrix for DNA sequences. It will be shown that the  
112 proposed system has high specificity and sensitivity for addressable DNA detection  
113 on a chip, which opens the door to the application of MOF functionalized silicon-based  
114 photoelectrochemical devices in spatially resolved (bio)chemical sensing.

## 115 2. Experimental

### 116 2.1 Materials

117 Double polished silicon (100) (boron doped, 1-10  $\Omega$ -cm, 475  $\mu$ m) wafers were  
118 purchased from Tianjing Yucai optic technology CO, China. All chemicals used for  
119 MOF synthesis were obtained commercially from Aladdin Reagents. Bovine serum  
120 albumin (BSA) and sodium dodecyl sulfate (SDS) were purchased from Sigma. All  
121 solutions were prepared using ultrapure water (18.2 M $\Omega$ -cm). The sequences of a  
122 25-mer probe, target and mismatched ssDNA molecules used in this study were  
123 purchased from Takara (Japan). The probe ssDNA was dissolved in pure water, while  
124 the cDNA and nDNA for hybridization were dissolved in 10 mM phosphate buffer with  
125 100 mM NaCl. The sequences are as follows: Probe ssDNA: 5'-GCAGT TGATC  
126 CTTTG GATAC CCTGG-3', or 5'-FITC- GCAGT TGATC CTTTG GATAC CCTGG-3';  
127 target complementary DNA (cDNA): 5'-CCAGG GTATC CAAAG GATCA ACTGC-3',  
128 or 5'- Texas Red- CCAGG GTATC CAAAG GATCA ACTGC-3'; non-complementary  
129 DNA (nDNA): 5'-CTCAG CCCTC TTCAA AAAC TCTCC A-3', or 5'- Texas Red-  
130 CTCAG CCCTC TTCAA AAAC TCTCC A-3'.

### 131 2.2 Silicon electrode preparation and modification

132 Double polished p-silicon (100) was used as the electrode. To obtain an ohmic  
133 contact, 30 nm Cr and 150 nm Au were thermally evaporated onto the rear side of  
134 silicon and subsequently heated to 300  $^{\circ}$ C for 5 min. Then the wafer was cut into 1.5  
135 cm  $\times$  1.5 cm pieces and cleaned in an ultrasonic bath with acetone, isopropyl alcohol,  
136 and ultrapure (Milli-Q) water before use.

137 Nano UIO-66-NH<sub>2</sub> was synthesized according to the published procedure (Wang et al.  
138 2017). First, 108 mg (0.3 mmol) amino-terephthalic acid and 60  $\mu$ L triethylamine were  
139 dissolved in 10 mL dimethylformamide (DMF), while 113.6 mg (0.3 mmol) ZrCl<sub>4</sub> and  
140 2.8 mL acetic acid were dissolved in 10 mL DMF, respectively. Then the two solutions  
141 were mixed and stirred at room temperature for 1 h. Finally, the mixed solution was  
142 transferred into a Teflon reactor chamber with the cleaned silicon substrate and kept  
143 in a 120  $^{\circ}$ C oven for 24 h. The silicon substrate modified with UIO-66-NH<sub>2</sub> was  
144 washed consecutively with copious amounts of DMF, methanol and water. A scanning  
145 electron microscope (SEM, TESCAN, MALA3 LMH) and X-ray diffraction (XRD,  
146 Bruker, D8 ADVANCE) were used to characterize the prepared nanoparticles.

### 147 2.3 DNA immobilization and hybridization

148 For probe DNA immobilization, 4 spots on one MOF-Si substrate were incubated with  
149 5  $\mu$ L of 5  $\mu$ M, 2  $\mu$ M, 0.5  $\mu$ M and 0.1  $\mu$ M probe ssDNA solutions for 30 min at room

150 temperature. Then the sensor surface was washed 3 times with pure water to remove  
151 any non-attached molecules. Before the detection of target DNA, the sensor  
152 substrate was incubated in a solution of 1% BSA + 0.05% SDS for 2 h at room  
153 temperature to prevent non-specific binding. Then the BSA-blocked sensor spots  
154 were exposed to 5  $\mu$ L hybridization solutions containing different concentrations of  
155 target cDNA (from 0.2 nM to 2  $\mu$ M) or 2  $\mu$ M mismatched ssDNA, respectively, for 30  
156 min at room temperature, followed by washing 3 times with pure water. The  
157 incubation processes were all performed in a closed Petri dish with a moistened  
158 tissue to prevent the small amount of DNA solutions from drying.

#### 159 *2.4 DC photocurrent measurements*

160 A laser (Thorlabs,  $\lambda = 405$  nm, max. 20 mW) controlled by LDC202C controller  
161 (Thorlabs) was used as the light source for activation. DC photocurrents were  
162 detected by a potentiostat analyser (Zennium, Zahner Elektrik, Germany). Linear  
163 sweep voltammetry (LSV) was carried out in 10 mM pH 7.4 phosphate buffered saline  
164 (PBS, 137 mM NaCl, 2.7 mM KCl, 10 mM Na<sub>2</sub>HPO<sub>4</sub>, 2 mM KH<sub>2</sub>PO<sub>4</sub>) with a scan rate  
165 of 5 mV/s. Chronoamperometry was carried out in 10 mM pH 7.4 PBS with the laser  
166 chopped at 0.1 Hz. For all measurements, a platinum electrode and an Ag/AgCl  
167 electrode were used as the counter and reference electrodes, respectively.

#### 168 *2.5 MLAE measurements*

169 The MLAE setup is shown in Fig. 1. A laser diode module (Thorlabs,  $\lambda = 405$  nm, max.  
170 20 mW) controlled by LDC202C controller (Thorlabs) was used for the generation of  
171 charge carriers. The diameter of the laser beam illuminated on the sensor surface is  
172 around 0.7 mm. The testing chamber was designed to have 6 holes with a diameter  
173 of 1 mm and 1.5 mm spacing at the bottom, resulting in 6 measurement spots on one  
174 electrode. These spots can be addressed by moving the silicon electrode mounted  
175 onto the PILine® XY stage (U723.25, Physik Instrumente (PI Shanghai) Co., Ltd.)  
176 with 10 nm sensor resolution and 0.1  $\mu$ m minimum incremental motion. Since the  
177 diameter of the laser spot is smaller than that of the sensing spots, by adjusting the  
178 positioning stages, the laser beam can just illuminate one of the sensing wells. The  
179 AC photocurrent was measured using a SR830 lock-in amplifier. A platinum electrode  
180 and an Ag/AgCl electrode moved with the working electrode were used as the  
181 counter and reference electrodes, respectively. For pH sensitivity measurements a  
182 range of 10 mM phosphate buffer (pH 4-9) with 0.1 M NaCl were used. For DNA  
183 sensing, 10 mM pH 7.4 PBS was adopted. The control program used for the  
184 measurements was written in LabView.

## 185 **3. Results and discussion**

### 186 *3.1 Photoelectrochemical responses of a p-type silicon electrode*

187 To investigate the effect of the modulation frequency on the AC photocurrent, the  
188 photocurrent and background current in the dark at 0.7 V, were measured from 5 to  
189 10,000 Hz in pH 7.4 PBS. As shown in Fig. 2a, the AC photocurrent increased with the  
190 frequency, while the dark current stayed constant at instrumental noise level. A high  
191 signal-to-noise ratio (SNR) of the photocurrent can be obtained with a frequency  
192 higher than 100 Hz. The result differs from the ITO-based electrode with an optimized  
193 frequency of 10 Hz (Wu et al. 2019; Zhang et al. 2017b), indicating that silicon would  
194 be a more **promising** electrode material for high speed measurements. 1 kHz was  
195 chosen as the measurement frequency in this work. Figs. 2b and 2c show the AC and  
196 DC *I-V* curves of silicon at 1 kHz in pH 7.4 PBS. The shape of the AC *I-V* curve for  
197 MLAE (Fig. 2b) was analogous to the typical *I-V* curve for a p-doped LAPS, which  
198 consists of three regions of accumulation, depletion and inversion (Wagner and  
199 Schöning 2007). The AC dark current was significantly smaller than the photocurrent  
200 (Fig. 2b), while the DC background current was comparable to the photocurrent for  
201 cathodic potentials up to -0.6 V (Fig. 2c), revealing a much higher SNR of MLAE for  
202 photoelectrochemical measurements.

203 A comparison of AC *I-V* curves of silicon with and without an insulator is presented in  
204 Fig. 3a. Due to the absence of insulator, the *I-V* curve of the bare silicon substrate is  
205 steeper and displays a greater photocurrent resulting in a higher sensitivity of  
206 photocurrent measurements. Figs. 3b and 3c show pH responses of the bare silicon  
207 in a series of pH PBS (10 mM, 0.1 M NaCl, pH 4-9) using MLAE and the  
208 corresponding calibration plot. An average pH sensitivity of about 47 mV/pH was  
209 obtained, which was higher than that of the traditional LAPS insulated with 70 nm  
210 SiO<sub>2</sub> (31 mV/pH, see Supporting Information, Fig. S1). Referring to our previous  
211 report (Zhang et al. 2017b), the sensitivity is due to the pH dependent kinetics of the  
212 faradaic process on the silicon surface. Since the silicon is p-type, the current is  
213 cathodic and it can be attributed to the reduction of H<sup>+</sup>.

### 214 *3.2 Surface modification with MOF nanoparticles*

215 MOF has been shown to be a great platform for the adsorption of DNA (Liu et al. 2012;  
216 Tian et al. 2015; Zhang et al. 2014; Zhao et al. 2016). UIO-66-NH<sub>2</sub> was chosen to  
217 decorate silicon as it is highly stable in water and biocompatible in biological system  
218 compared to other kinds of MOF materials (Ruyra et al. 2015). In addition, the  
219 electrostatic attractions such as  $\pi$ - $\pi$  stacking or hydrogen bond interactions between  
220 UIO-66-NH<sub>2</sub> and the aromatic nucleotide bases of DNA facilitate efficient and  
221 high-affinity binding (Wang et al. 2017). The successful preparation of MOF

222 nanoparticles on silicon was confirmed in SEM images (Figs. 4a and 4b). It was  
223 shown the nanoparticles with an average diameter of  $150 \pm 20$  nm were uniformly  
224 distributed over the silicon surface without aggregation. The particles showed regular  
225 octahedron structure, which was the typical shape of UIO-66-NH<sub>2</sub> based MOF. The  
226 percentage surface coverage of MOF nanoparticles on silicon was estimated using  
227 ImageJ. An average surface coverage of  $70\% \pm 3.2\%$  (SD) with 6 batches of samples  
228 was obtained, indicating a reliable immobilization protocol. Typical X-ray diffraction  
229 (XRD) measurements were used to establish the crystal phase of the UIO-66-NH<sub>2</sub>. As  
230 shown in Fig 4c, all the diffraction peaks of the MOF powder corresponded well to the  
231 simulated pattern derived from the single-crystal X-ray diffraction data. As shown in  
232 Fig. 4c, the XRD pattern collected for UIO-66-NH<sub>2</sub> grown on silicon (trace B) agreed  
233 well with the powder XRD pattern (trace A) in terms of some main peaks,  
234 demonstrating the formation of pure-phase UIO-66-NH<sub>2</sub>.

235 As there is unlikely to be any chemical reaction between UIO-66-NH<sub>2</sub> and silicon,  
236 MOF nanoparticles are physically adsorbed on the silicon surface. Fig S2a shows the  
237 effect of MOF adsorption on the AC photocurrent output of the sensor platform. After  
238 the modification of silicon with MOF, the *I-V* curve measured with laser illumination  
239 shifted and the photocurrent decreased significantly, which may be attributed to the  
240 positive charge and poor conductivity of UIO-66-NH<sub>2</sub> MOF. On the other hand, the  
241 dark current stayed significantly smaller and showed almost no change due to MOF  
242 immobilization. The stability of the MOF-modified silicon electrode (MOF-Si) was  
243 evaluated using AC *I-V* measurements. Fig. S2b shows potential shifts of *I-V* curves in  
244 PBS for the MOF-Si and Si electrodes measured over 5 h. One can see that there  
245 was only small perturbation of *I-V* curves for the MOF-Si sample, while obvious shifts  
246 were observed for the bare Si electrode, indicating a passivation effect resulting from  
247 the modification with MOF nanoparticles.

### 248 3.3 Probe ssDNA adsorption on MOF-Si

249 MOF-Si and bare silicon substrates were incubated respectively with a drop (5  $\mu$ l) of 2  
250  $\mu$ M probe single-stranded (ss)DNA labelled with FITC. The incubation process was  
251 performed in a closed Petri dish with a moistened tissue to prevent the small amount  
252 of DNA solutions from drying. Then the substrates were washed 3 times with pure  
253 water to remove any non-attached DNA molecules. As displayed in Fig. 5a, the  
254 MOF-Si surface exhibited strong fluorescence emission with the presence of the  
255 probe FITC-ssDNA, while bare silicon showed insignificant fluorescence (data not  
256 shown), demonstrating the feasibility of amine-functionalized MOF as a great platform  
257 for DNA adsorption. The strong binding is probably due to the electrostatic attraction  
258 as DNA carries negative charge while UIO-66-NH<sub>2</sub> showed a slightly positive zeta  
259 potential ( $\sim 3.4$  mV). After DNA adsorption, the zeta potential changed to  $-6.7$  mV,  
260 which was consistent to the result shown in (Wang et al. 2017). Moreover, the addition  
261 of acetic acid introduces additional defects in UIO-66-NH<sub>2</sub>, which are also beneficial  
262 for DNA binding (Wang et al. 2017).



263 To investigate the effect of the probe ssDNA concentration on the MLAE signal, the  
264 probe molecules were immobilized from solutions of 0.1  $\mu\text{M}$ , 0.5  $\mu\text{M}$ , 2  $\mu\text{M}$  and 5  $\mu\text{M}$   
265 ssDNA. The  $I$ - $V$  curve shifted from 20 mV to 46 mV with increasing ssDNA  
266 concentration from 0.1  $\mu\text{M}$  to 2  $\mu\text{M}$  and stayed almost stable beyond 2  $\mu\text{M}$  (Fig. S3a).  
267 As the optimized result, 2  $\mu\text{M}$  probe ssDNA was chosen for immobilization in our next  
268 experiments. Again, there is no effect of DNA adsorption on the dark current (see Fig.  
269 S2a). Fig. 5b shows  $I$ - $V$  curves before and after probe ssDNA adsorption measured  
270 with 405 nm laser. A positive shift (or an increase of photocurrent) was observed,  
271 which was opposite to that of conventional LAPS (Wang et al. 2015; Wu et al. 2015).  
272 The main difference in the two techniques is the absence of an insulator layer in  
273 MLAE, resulting in the generation of a redox current on the semiconductor electrode  
274 (Wu et al. 2019). Figs. 5c and 5d illustrate the photocurrent changes with chopped  
275 light (0.1 Hz) at -0.6 V measured with a potentiostat. For  $\text{SiO}_2$ -Si, only capacitive  
276 current spikes were observed due to the charge and discharge of the depletion layer  
277 of Si with the light switched on and off (Fig. 5c). On the other hand, the MOF-Si  
278 electrode showed a combination of capacitive current and photocatalytic redox  
279 current (Fig. 5d in black). Since DNA is negatively charged, it would increase the  
280 surface concentrations of hydrogen ions at the electrode and accelerate the cathodic  
281 reduction process, thus resulting in a higher redox current compared to the sensor  
282 surface without DNA (see Fig. 5d in red). This indicates that the sensitivity of MLAE  
283 can extend to charges in the diffusion layer ( $\sim \mu\text{m}$ ), which is no longer limited to  
284 Debye length ( $\sim 0.7$  nm in the PBS buffer) induced by counter-ion screening effects as  
285 that of traditional field-effect devices.

### 286 3.4 Target ssDNA detection using MLAE

287 The non-specific adsorption of target DNA on probe ssDNA-MOF-Si was investigated.  
288 Fig S3b shows the  $I$ - $V$  curves before and after hybridization with 2  $\mu\text{M}$  complementary  
289 and non-complementary DNA (cDNA, nDNA). The hybridization with cDNA (2  $\mu\text{M}$ )  
290 results in a greater positive shift of the  $I$ - $V$  curves or a higher photocurrent signal at  
291 the depleted semiconductor. As mentioned above, this increase in photocurrent is  
292 attributed to the electrostatic attraction of hydrogen ions to the negatively charged  
293 cDNA. For the case of nDNA, a smaller but significant increase in photocurrent was  
294 also observed (see Fig. S3b), indicating the non-specific adsorption of target DNA on  
295 the sensor surface.

296 As a good antifouling agent, BSA was used to prevent non-specific binding of target  
297 DNA on the sensor interface. Photocurrent measurements showed that BSA  
298 adsorption did not affect cDNA binding and sensing, while the non-specific binding of  
299 nDNA was significantly reduced (Fig 6a). This is also demonstrated through  
300 fluorescent images of DNA with and without BSA incubation (Fig. S4).

301 The BSA-blocked 6 spots on one semiconductor electrode were exposed to 5  $\mu\text{L}$   
302 hybridization solutions with different concentrations of target cDNA (0.2 nM, 2 nM, 20



303 nM, 200 nM, 2  $\mu$ M) or 2  $\mu$ M mismatched ssDNA, respectively, for 30 min at room  
304 temperature. Fig. 6b presents the dependence of the hybridization signal of MOF-Si  
305 on the target cDNA concentration ranging from 0.2 nM to 2  $\mu$ M on one chip. The  
306 hybridization signal increases with increasing target cDNA concentration and  
307 achieves a value of 34 mV at 2  $\mu$ M cDNA. At a very low cDNA concentration of 0.2 nM,  
308 a detectable hybridization signal of 4 mV was registered, which is similar to the shift  
309 resulting from nDNA adsorption with a much higher concentration (2  $\mu$ M vs. 0.2 nM).  
310 These results indicate a good specificity and sensitivity of the developed technique  
311 allowing the successful discrimination between target DNA analytes with different  
312 concentration on one semiconductor electrode. For specific applications, further  
313 investigations such as the effect of single mismatched DNA will be required for the  
314 exploitation of the new sensor platform.

#### 315 **4. Conclusions**

316 Modulated light-activated electrochemistry (MLAE) based on AC photocurrent  
317 measurements at metal-organic frameworks (MOFs) functionalized silicon was  
318 developed for addressable DNA detection. The AC measurements showed a higher  
319 signal-to-noise ratio (SNR) of photocurrents and a steeper photocurrent-voltage (*I-V*)  
320 curve compared to the related techniques of LAE and LAPS. In addition, the  
321 proposed system was proven to be a robust platform for spatially resolved detection  
322 of DNA molecules. Metal-organic framework (MOF) nanoparticles (UIO-66-NH<sub>2</sub>) were  
323 deposited on silicon electrodes for probe DNA immobilization. The *I-V* results showed  
324 that the hybridization signal of complementary DNA (cDNA) increases from 4 mV to  
325 34 mV with increasing the concentration of cDNA from 0.2 nM to 2  $\mu$ M on one chip. In  
326 contrast, a small signal of 5 mV was recorded for the non-complementary DNA  
327 adsorption (5  $\mu$ M). This example demonstrated the potential of MOF functionalized  
328 MLAE as a simple and low-cost platform for multi-spot and label-free bio(chemical)  
329 molecule detection with good sensitivity and specificity.

#### 330 **Acknowledgments**

331 This work was supported by the National Natural Science Foundation of China (Grant No.  
332 31800827, 31661143030, 51861145307), Shanxi Provincial Natural Science Foundation  
333 (Grant No. 2018JQ8058), the Doctoral Fund of Education Ministry of China (Grant No.  
334 2017M613146), and the Fundamental Research Funds for the Central Universities.

#### 335 **References**

336 Campbell, M., Dincă, M., 2017. Metal–Organic Frameworks as Active Materials in Electronic Sensor  
337 Devices. *Sensors* 17(5), 1108.  
338 Choudhury, M.H., Ciampi, S., Lu, X., Kashi, M.B., Zhao, C., Gooding, J.J., 2017. Spatially confined  
339 electrochemical activity at a non-patterned semiconductor electrode. *Electrochimica Acta* 242,

340 240-246.

341 Hafeman, D., Parce, J., McConnell, H., 1988. Light-addressable potentiometric sensor for biochemical  
342 systems. *Science* 240(4856), 1182-1185.

343 Licht, S., Myung, N., Sun, Y., 1996. A Light Addressable Photoelectrochemical Cyanide Sensor.  
344 *Analytical Chemistry* 68(6), 954-959.

345 Liu, S., Wang, L., Tian, J., Luo, Y., Chang, G., Asiri, A.M., Al-Youbi, A.O., Sun, X., 2012. Application of  
346 Zeolitic Imidazolate Framework-8 Nanoparticles for the Fluorescence-Enhanced Detection of Nucleic  
347 Acids. *ChemPlusChem* 77(1), 23-26.

348 Ma, W., Jiang, Q., Yu, P., Yang, L., Mao, L., 2013. Zeolitic Imidazolate Framework-Based Electrochemical  
349 Biosensor for in Vivo Electrochemical Measurements. *Analytical Chemistry* 85(15), 7550-7557.

350 Macazo, F.C., White, R.J., 2016. Bioinspired Protein Channel-Based Scanning Ion Conductance  
351 Microscopy (Bio-SICM) for Simultaneous Conductance and Specific Molecular Imaging. *Journal of the  
352 American Chemical Society* 138(8), 2793-2801.

353 Meng, W., Wen, Y., Dai, L., He, Z., Wang, L., 2018. A novel electrochemical sensor for glucose detection  
354 based on Ag@ZIF-67 nanocomposite. *Sensors and Actuators B: Chemical* 260, 852-860.

355 Meng, W., Xu, S., Dai, L., Li, Y., Zhu, J., Wang, L., 2017. An enhanced sensitivity towards H<sub>2</sub>O<sub>2</sub> reduction  
356 based on a novel Cu metal-organic framework and acetylene black modified electrode. *Electrochimica  
357 Acta* 230, 324-332.

358 Obien, M.E.J., Deligkaris, K., Bullmann, T., Bakkum, D.J., Frey, U., 2015. Revealing neuronal function  
359 through microelectrode array recordings. *Frontiers in Neuroscience* 8, 423-423.

360 Perry, D., Page, A., Chen, B., Frenguelli, B.G., Unwin, P.R., 2017. Differential-Concentration Scanning  
361 Ion Conductance Microscopy. *Analytical Chemistry* 89(22), 12458-12465.

362 Poghosian, A., Schöning, M.J., 2014. Label-free sensing of biomolecules with field-effect devices for  
363 clinical applications. *Electroanalysis* 26(6), 1197-1213.

364 Polcari, D., Dauphin-Ducharme, P., Mauzeroll, J., 2016. Scanning Electrochemical Microscopy: A  
365 Comprehensive Review of Experimental Parameters from 1989 to 2015. *Chemical Reviews* 116(22),  
366 13234-13278.

367 Ruyra, À., Yazdi, A., Espín, J., Carné-Sánchez, A., Roher, N., Lorenzo, J., Imaz, I., MasPOCH, D., 2015.  
368 Synthesis, Culture Medium Stability, and In Vitro and In Vivo Zebrafish Embryo Toxicity of  
369 Metal-Organic Framework Nanoparticles. *Chemistry – A European Journal* 21(6), 2508-2518.

370 Seo, D., Lim, S.Y., Lee, J., Yun, J., Chung, T.D., 2018. Robust and High Spatial Resolution Light  
371 Addressable Electrochemistry Using Hematite ( $\alpha$ -Fe<sub>2</sub>O<sub>3</sub>) Photoanodes. *ACS Applied Materials &  
372 Interfaces* 10(39), 33662-33668.

373 Spira, M.E., Hai, A., 2013. Multi-electrode array technologies for neuroscience and cardiology. *Nature  
374 Nanotechnology* 8, 83.

375 Takahashi, Y., Shevchuk, A.I., Novak, P., Babakinejad, B., Macpherson, J., Unwin, P.R., Shiku, H., Gorelik,  
376 J., Klenerman, D., Korchev, Y.E., Matsue, T., 2012. Topographical and electrochemical nanoscale  
377 imaging of living cells using voltage-switching mode scanning electrochemical microscopy. *Proceedings  
378 of the National Academy of Sciences of the United States of America* 109(29), 11540-11545.

379 Tian, J., Liu, Q., Shi, J., Hu, J., Asiri, A.M., Sun, X., He, Y., 2015. Rapid, sensitive, and selective  
380 fluorescent DNA detection using iron-based metal-organic framework nanorods: Synergies of the  
381 metal center and organic linker. *Biosensors and Bioelectronics* 71, 1-6.

382 Tu, Y., Ahmad, N., Briscoe, J., Zhang, D.-W., Krause, S., 2018. Light-Addressable Potentiometric Sensors  
383 Using ZnO Nanorods as the Sensor Substrate for Bioanalytical Applications. *Analytical Chemistry*

384 90(14), 8708-8715.

385 Vogel, Y.B., Gooding, J.J., Ciampi, S., 2019. Light-addressable electrochemistry at semiconductor  
386 electrodes: redox imaging, mask-free lithography and spatially resolved chemical and biological  
387 sensing. *Chemical Society Reviews* 48(14), 3723-3739.

388 Wagner, T., Schöning, M.J., 2007. Chapter 5 Light-addressable potentiometric sensors (LAPS): recent  
389 trends and applications. In: Alegret, S., Merkoçi, A. (Eds.), *Comprehensive Analytical Chemistry*, pp.  
390 87-128. Elsevier.

391 Wang, J., Du, L., Krause, S., Wu, C., Wang, P., 2018. Surface modification and construction of LAPS  
392 towards biosensing applications. *Sensors and Actuators B: Chemical* 265, 161-173.

393 Wang, J., Zhou, Y., Watkinson, M., Gautrot, J., Krause, S., 2015. High-sensitivity light-addressable  
394 potentiometric sensors using silicon on sapphire functionalized with self-assembled organic  
395 monolayers. *Sensors and Actuators B: Chemical* 209, 230-236.

396 Wang, Z., Fu, Y., Kang, Z., Liu, X., Chen, N., Wang, Q., Tu, Y., Wang, L., Song, S., Ling, D., Song, H., Kong,  
397 X., Fan, C., 2017. Organelle-Specific Triggered Release of Immunostimulatory Oligonucleotides from  
398 Intrinsically Coordinated DNA–Metal–Organic Frameworks with Soluble Exoskeleton. *Journal of the  
399 American Chemical Society* 139(44), 15784-15791.

400 Wu, C., Bronder, T., Poghossian, A., Werner, C.F., Schöning, M.J., 2015. Label-free detection of DNA  
401 using a light-addressable potentiometric sensor modified with a positively charged polyelectrolyte  
402 layer. *Nanoscale* 7(14), 6143-6150.

403 Wu, C., Poghossian, A., Bronder, T.S., Schöning, M.J., 2016. Sensing of double-stranded DNA molecules  
404 by their intrinsic molecular charge using the light-addressable potentiometric sensor. *Sensors and  
405 Actuators B: Chemical* 229, 506-512.

406 Wu, F., Zhou, B., Wang, J., Zhong, M., Das, A., Watkinson, M., Hing, K., Zhang, D.-W., Krause, S., 2019.  
407 Photoelectrochemical imaging system for the mapping of cell surface charges. *Analytical Chemistry* 91,  
408 5896-5903.

409 Yang, Y., Ciampi, S., Zhu, Y., Gooding, J.J., 2016. Light-Activated Electrochemistry for the  
410 Two-Dimensional Interrogation of Electroactive Regions on a Monolithic Surface with Dramatically  
411 Improved Spatial Resolution. *The Journal of Physical Chemistry C* 120(24), 13032-13038.

412 Yang, Y., Cuartero, M., Gonçalves, V.R., Gooding, J.J., Bakker, E., 2018. Light-Addressable Ion Sensing for  
413 Real-Time Monitoring of Extracellular Potassium. *Angewandte Chemie International Edition* 57(51),  
414 16801-16805.

415 Yoshinobu, T., Miyamoto, K.-i., Wagner, T., Schöning, M.J., 2015. Recent developments of chemical  
416 imaging sensor systems based on the principle of the light-addressable potentiometric sensor. *Sensors  
417 and Actuators B: Chemical* 207, 926-932.

418 Yoshinobu, T., Miyamoto, K.-i., Werner, C.F., Poghossian, A., Wagner, T., Schöning, M.J., 2017.  
419 Light-addressable potentiometric sensors for quantitative spatial imaging of chemical species. *Annual  
420 Review of Analytical Chemistry* 10(0), 225-246.

421 Zhang, C., Wang, X., Hou, M., Li, X., Wu, X., Ge, J., 2017a. Immobilization on Metal–Organic Framework  
422 Engenders High Sensitivity for Enzymatic Electrochemical Detection. *ACS Applied Materials &  
423 Interfaces* 9(16), 13831-13836.

424 Zhang, D.-W., Wu, F., Krause, S., 2017b. LAPS and SPIM imaging using ITO-coated glass as the substrate  
425 material. *Analytical Chemistry* 89(15), 8129-8133.

426 Zhang, H.-T., Zhang, J.-W., Huang, G., Du, Z.-Y., Jiang, H.-L., 2014. An amine-functionalized  
427 metal–organic framework as a sensing platform for DNA detection. *Chemical Communications* 50(81),

428 12069-12072.  
429 Zhao, H.-Q., Qiu, G.-H., Liang, Z., Li, M.-M., Sun, B., Qin, L., Yang, S.-P., Chen, W.-H., Chen, J.-X., 2016. A  
430 zinc(II)-based two-dimensional MOF for sensitive and selective sensing of HIV-1 ds-DNA sequences.  
431 *Analytica Chimica Acta* 922, 55-63.

432 Figure captions:

433 Fig. 1 Experimental scheme of silicon-based MLAE.

434 Fig. 2 (a) The frequency dependence of the AC photocurrent (red) and background  
435 AC current in the dark (black) biased at -0.6 V. (b) AC current-voltage (*I-V*) curves  
436 measured with lock-in amplifier (1 kHz) and (c) DC *I-V* curves measured with a  
437 potentiostat with a 405 nm laser (red) and dark (black). **Each data point is an average  
438 of the 6 measurements on 6 sensing spots on one electrode and is presented as  
439 mean  $\pm$  SD.**

440 Fig. 3 (a) AC *I-V* curves of p-silicon substrates with and without insulator measured  
441 with the same laser intensity. **Each data point is an average of the 6 measurements  
442 on 6 sensing spots on one electrode and is presented as mean  $\pm$  SD.** (b) AC *I-V*  
443 curves at different pH values and (c) corresponding calibration plot.

444 Fig. 4 Typical SEM top view of UIO-66-NH<sub>2</sub> nanoparticles grown on p-Si (100) surface  
445 (a) overview and (b) zoomed images. (c) **XRD patterns for simulated UIO-66-NH<sub>2</sub>,  
446 UIO-66-NH<sub>2</sub> powder and UIO-66-NH<sub>2</sub> grown on bare silicon.**

447 Fig. 5 (a) Fluorescence image taken from MOF-Si surface after incubated with a drop  
448 of 2  $\mu$ M FITC-labelled probe ssDNA solution; (b) AC *I-V* curves measured before and  
449 after the probe ssDNA adsorption. Each data point is an average of the 6  
450 measurements and is presented as mean  $\pm$  SD. *I-t* curves measure with potentiostat  
451 at -0.6 V with a chopped laser illumination of 0.1 Hz on (c) SiO<sub>2</sub>-Si and on (d) MOF-Si  
452 without (black) and with (red) probe DNA adsorption.

453 Fig. 6 AC *I-V* curves recorded (a) from a single channel before and after ssDNA  
454 adsorption, after incubation with BSA, after non-specific adsorption of nDNA, and  
455 after hybridization with cDNA; (b) from five channels modified with 2  $\mu$ M probe ssDNA  
456 when exposed to serial concentrations of concentrations of cDNA (0.2 nM, 2 nM, 20  
457 nM, 200 nM and 2  $\mu$ M, respectively) and (c) the corresponding statistical results of the  
458 hybridization signals of the MLAE in response to different cDNA concentrations. The  
459 mean and stand error of the mean (SEM) of three experiments are shown.

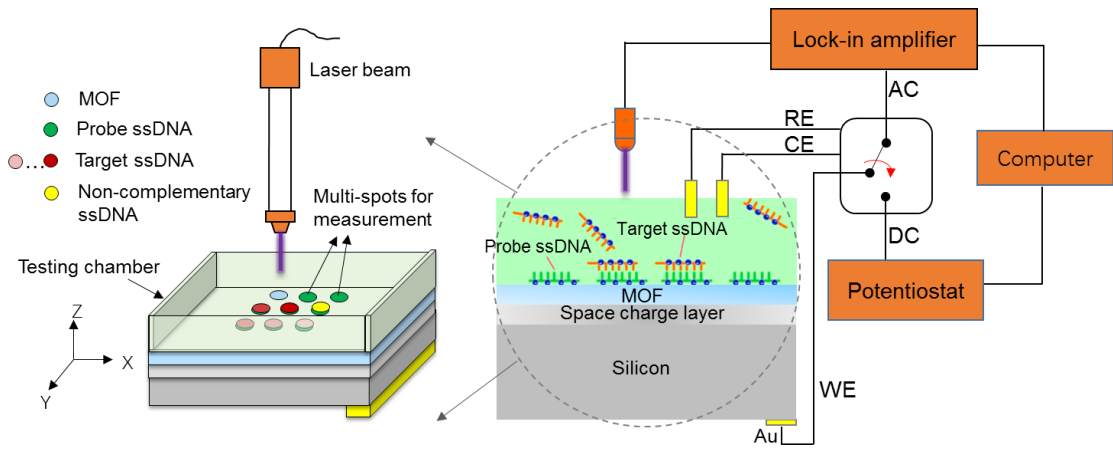


Fig. 1

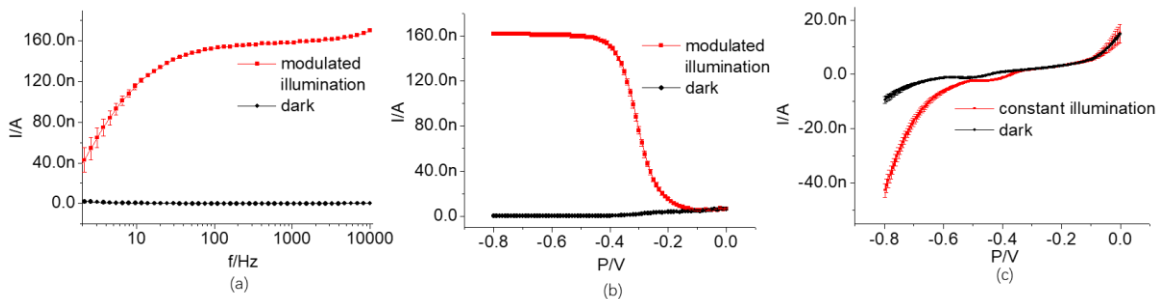


Fig. 2

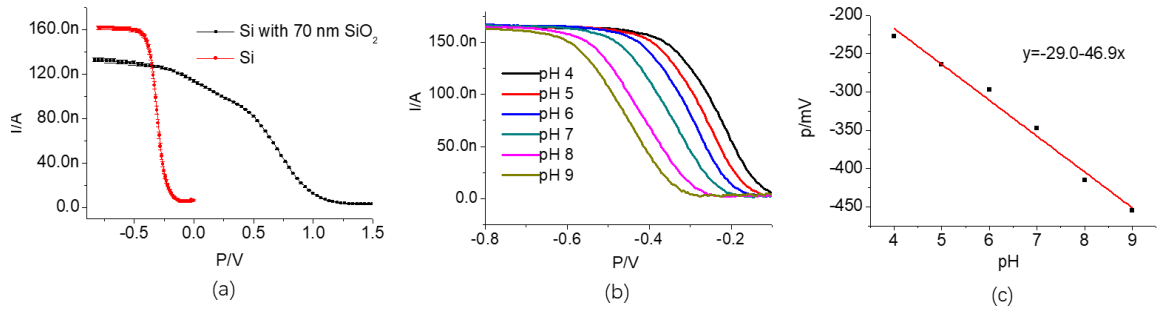
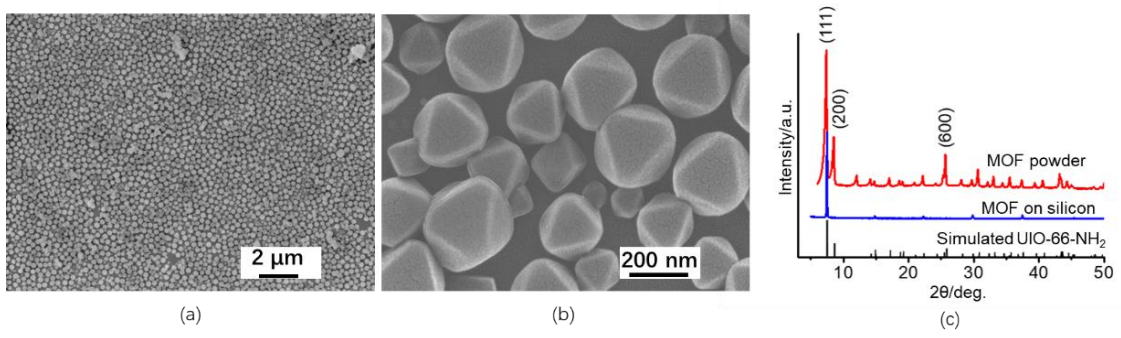
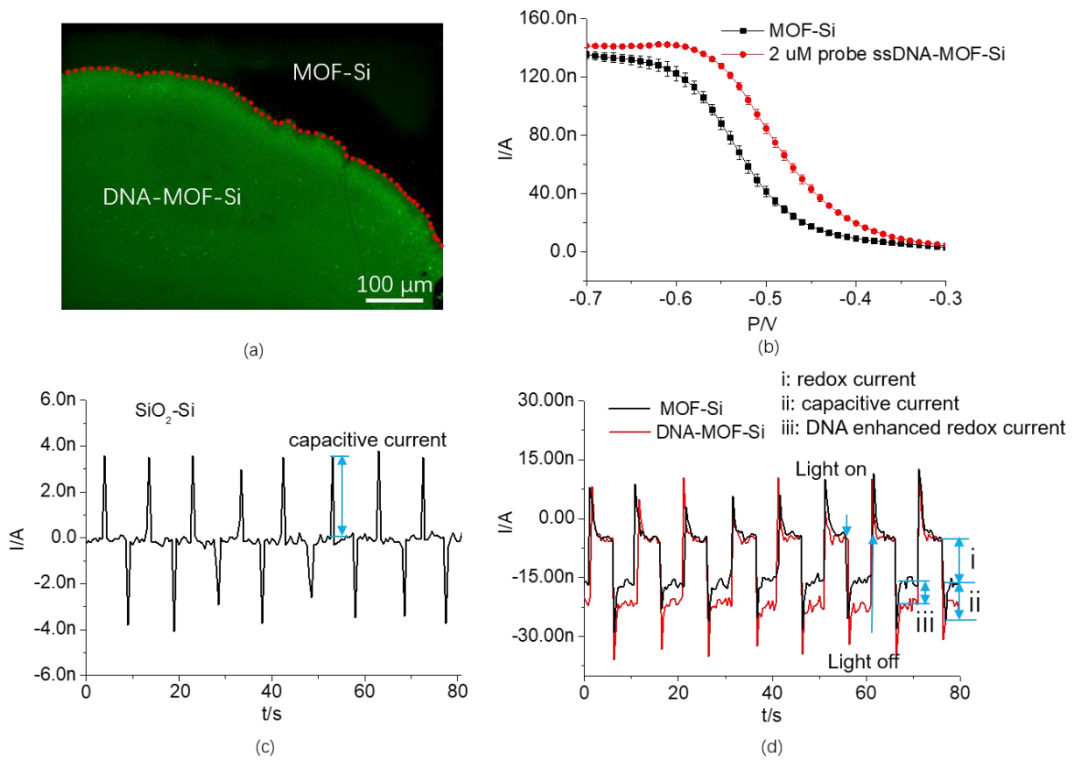


Fig. 3



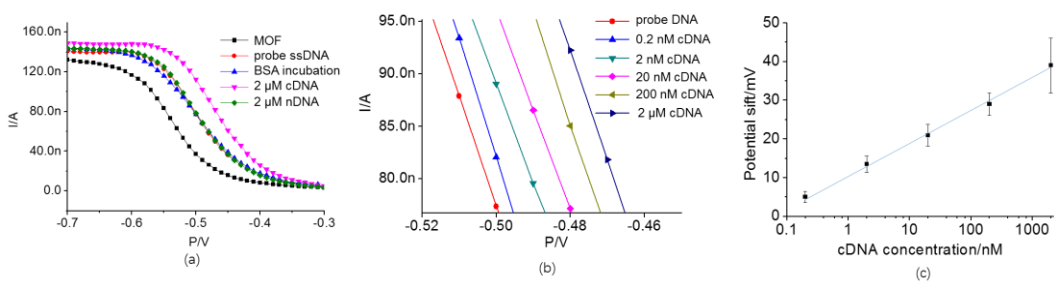
467  
468

Fig. 4



469  
470

Fig. 5



471  
472

Fig. 6



## CRediT Author Statement

**Jian Wang:** Data curation, Formal analysis, Methodology, Writing- original draft, Writing - review & editing. **Zhao Yang:** Data curation, Formal analysis, Resources. **Wei Chen:** Methodology, Software, Conceptualization. **Liping Du:** Investigation, Methodology, Validation. **Bo Jiao:** Investigation, Resources. **Steffi Krause:** Conceptualization, Writing - review & editing. **Ping Wang:** Funding acquisition, Project administration. **Quipping Wei:** Investigation, Methodology. **De-Wen Zhang:** Conceptualization, Formal analysis, Project administration, Supervision, Writing - review & editing. **Chunsheng Wu:** Resources, Funding acquisition, Supervision, Writing - review & editing.

**Supplementary Material**

[Click here to download Supplementary Material: Revised Supplementary Materials 20190828.docx](#)

## Highlights:

- Modulated light-activated electrochemistry at silicon for addressable biosensing
- A local AC photocurrent showed a higher signal-to-noise ratio than the DC response
- Metal-organic frameworks nanoparticles were grown in-situ to stabilize the surface
- The photocurrent increased as the enhanced reduction process after DNA binding
- This work provided a promising platform for multi-spot and label-free DNA chips

**Declaration of interests**

The authors declare that they have no known competing financial interests or personal relationships that could have appeared to influence the work reported in this paper.

The authors declare the following financial interests/personal relationships which may be considered as potential competing interests: